JTTEE5 20:307–316
DOI: 10.1007/s11666-010-9597-6
1059-9630/$19.00 © ASM International

Effect of Using Liquid Feedstock in a High Pressure Cold Spray Nozzle

E. Farvardin, O. Stier, V. Lüthen, and A. Dolatabadi

(Submitted May 6, 2010; in revised form October 15, 2010)

This study investigates the effect of water injection in the high pressure chamber of a cold spray nozzle. A De Laval nozzle geometry with constant back pressure and temperature is modeled numerically using Reynolds Stress Model coupled equations. Water spray with a droplet size of 10-100 μm is modeled using both uniform and Rosin-Rammler size distributions. The two-phase flow of gas-liquid is modeled using an unsteady discrete phase mass source with two-way coupling with the main gas flow. Upon injection, the droplets in the water spray evaporate while travelling through the nozzle due to momentum and energy exchange with the gas flow. The evaporation behavior in the presence of water content is modeled and a correlation between the initial diameter and the diameter just before the throat is obtained. As a result, the proper droplet size distribution with a fully evaporative spray can be used as a carrier of nano-particles in cold spray nozzles. Having the results, guides us to substitute the un-evaporated part of the droplet with an equal diameter agglomerate of nano-particles and find a minimum fraction of nano-particles suspended in the liquid which guarantees fully evaporative liquid spray injection.

Keywords cold spray process, discrete phase model, liquid feedstock, nano-particle, spray evaporation, suspension

1. Introduction

Suspension sprays have been extensively used in spray drying processes of food, pharmaceutical, and cosmetic industries for more than a century (Ref 1). In recent years, the use of suspension sprays in thermal spraying processes has been started as an outstanding vehicle for deposition of sub-micron-sized particles (Ref 2). In fact, coatings made of nano-particles have shown outstanding characteristics in a vast range of applications, i.e., aerospace, turbomachinery blades, machining, etc. Among improved advantages of nano-sized coatings are better corrosion protection, augmentation of composite strength (Ref 3), fire protection, water resistance (Ref 4), and high endurance (Ref 5). The main issue with direct nano-particle injection in thermal spray nozzles is feeding of nano-particles due to their agglomeration and clogging in the feeding tubes (Ref 6). To overcome the agglomeration problem, using suspension of nano-particles in a neutral liquid has recently being employed, which allows using very fine particles for thermal spray coatings (Ref 7).

In suspension thermally sprayed coatings, the coating material in the form of particles of size 30 to 200 nm is dispersed in a liquid carrier (e.g., water) and then the suspension is injected into the main gas flow. The suspension spray then travels in the high temperature flow, and its liquid part, evaporates along its trajectory. The remaining solid part of the spray which usually appears as fine agglomerates of nano-particles is accelerated to be deposited on the substrate (Ref 8). A restriction of this method is that the suspension spray must be totally evaporated before the deposition on the substrate. Therefore, the evaporation rate of suspension particles has a considerable effect on the coating process. In HVOF and plasma thermal spray, because of high temperatures associated with the gaseous field, the evaporation rate is very high and fully evaporated spray is somehow guaranteed, but in a cold spray nozzle the evaporation rate is a crucial parameter for having a nano-particle suspension coating. In addition, the heat exchange between droplets and the main gaseous flow may affect the downstream flow field of the nozzle.

In this article, the effect of water injection into the high pressure chamber of the commercial cold spray nozzle type "v24" by CGT GmbH, Ampfing, Germany, is simulated to study its effect on the main flow and its rate of evaporation. Although the rate of evaporation of homogeneous water spray might be somehow different from the evaporation of suspension spray, the results can be used as

This article is an invited paper selected from presentations at the 2010 International Thermal Spray Conference and has been expanded from the original presentation. It is simultaneously published in *Thermal Spray: Global Solutions for Future Applications, Proceedings of the 2010 International Thermal Spray Conference*, Singapore, May 3-5, 2010, Basil R. Marple, Arvind Agarwal, Margaret M. Hyland, Yuk-Chiu Lau, Chang-Jiu Li, Rogerio S. Lima, and Ghislain Montavon, Ed., ASM International, Materials Park, OH, 2011.

E. Farvardin and **A. Dolatabadi**, Department of Mechanical & Industrial Engineering, Concordia University, Montreal, Canada; and **O. Stier** and **V. Lüthen**, Siemens AG, Corporate Technology, CT MM 5, Siemensdamm 50, 13629 Berlin, Germany. Contact e-mails: dolat@encs.concordia.ca and dolat@me.concordia.ca.

List of symbols

A_d	Droplet surface area, m^2	r	Radial coordinate, m
a	Speed of sound, m/s	Sc	Schmidt number
B	Spalding mass transfer number	Sh	Sherwood number
C_s	Vapor concentration at droplet surface, $kgmol/m^3$	T	Gas temperature, K
		T_d	Droplet temperature, K
C_∞	Vapor concentration in the bulk gas, $kgmol/m^3$	t	Time, s
C_D	Drag coefficient	v	Gas velocity, m/s
c_p	Specific heat of water, J/kg · K	v_d	Droplet velocity, m/s
D	Diffusivity, m^2/s	X_d	Percentage of droplet sizes having diameter smaller than d
d	Droplet diameter, m		
h	Convective heat transfer coefficient, $W/m^2 \cdot K$	x	Axial coordinate, m
k	Gas conductivity, W/m · K	Y^*	Mass fraction of liquid at droplet surface
L	Evaporation latent heat of water, J/kg	Y_l	Mass fraction of liquid at the bulk gas
M_d	Droplet Mach number	y	Non-dimensionalized distortion of droplets
m_d	Droplet mass, kg	ε_p	Droplet emissivity
m_g'	Gas mass flow rate, kg/s	θ_R	Radiation temperature, K
m_l'	Total liquid mass flow rate, kg/s	κ	Stefan-Boltzman constant (5.67×10^{-8} $W/m^2 \cdot K^4$)
Nu_d	Droplet Nusselt number		
P	Gas pressure, Pa	μ	Molecular viscosity, kg/m · s
P_l^{sat}	Saturation pressure of liquid, Pa	ρ	Gas density, kg/m^3
Pr	Prandtl number	ρ_d	Droplet density, kg/m^3
R	Droplet radius, m	σ	Droplet surface tension, kg/s^2
Re_d	Droplet Reynolds number		

a first approximation for finding the droplet distribution which results in complete evaporation before the nozzle throat.

2. Geometry and Operating Conditions

In this study, the effect of using liquid feedstock in the CGT v24 cold spray nozzle is investigated. The nozzle has a circular cross section with an exit diameter of 6.58 mm and exit to throat area ratio of 5.9. The nozzle chamber before the converging section of the nozzle has a diameter of 14 mm. The injector has a diameter of 1 mm and is located 110 mm upstream the throat.

Nitrogen with a back pressure of 40 barg (bars gage) and temperature of 873 K is used as the process gas. The nozzle expands nitrogen from the high back pressure to a lower pressure at the nozzle exit. Water is injected at the mass flow rate of 1 g/s with the primary temperature of 300 K.

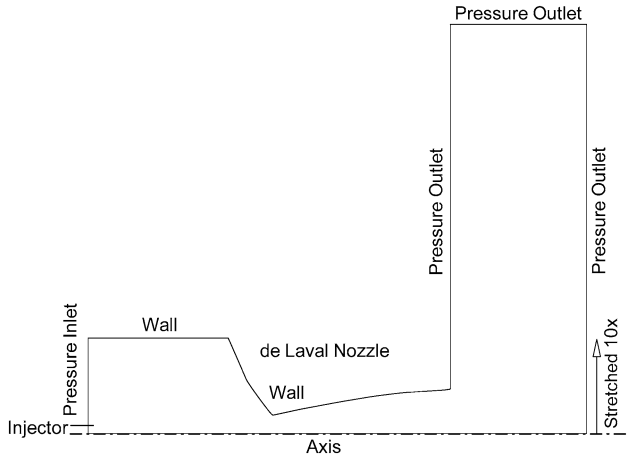

Fig. 1 Domain and boundary conditions of CGT v24 cold spray nozzle

3. Methodology

3.1 Boundary Conditions

The computational domain, as schematically shown in Fig. 1, is the same as the previous work of the group (Ref 9) and is composed of 1350 × 100 quadrilateral cells in the axial and radial directions, respectively. Outside the nozzle is also covered by 1400 × 100 quadrilateral cells in the axial and radial directions, respectively.

The injector is considered as a discrete injector composed of 10 points (see Fig. 2), delivering water at 300 K with different size distributions. The size distributions used in this article are 10, 30, or 50 μm uniform or 10-100 μm Rosin-Rammler distribution. It should be mentioned that Rosin-Rammler distribution is an exponential distribution in which droplet sizes, i.e., 10-100 μm, are to be divided into some intervals, and the percentage of droplet sizes less than a specified diameter can be found using Eq 1, mean diameter ($\bar{d}$) and spread parameter n. In this study, the value of mean diameter and spread parameter are considered 30 μm and 3.5, respectively.

$$X_d = 1 - \exp(-(d/\bar{d})^n) \quad \text{(Eq 1)}$$

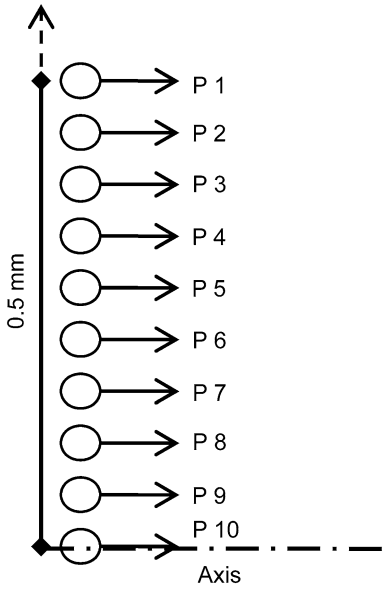

Fig. 2 Injector discrete phase model (DPM)

The boundary conditions are as follows. Adiabatic walls are used to model the nozzle and the chamber wall. The nozzle inlet for the gaseous part of the flow is considered to have a fixed and uniform pressure, i.e., 40 or 24 barg. Owing to the fact that in this study, the main aim is to find a general point of view of the effect of spray injection and not the deposition of the particles, the substrate is not modeled and the area outside the nozzle is considered as a free jet in a quiescent area. Hence at the right end of the geometry, an area with boundaries of fixed and uniform atmospheric pressure is applied.

3.2 Numerical Techniques

Having the mesh and boundary conditions, the numerical simulation is performed by the commercial software Fluent 6.3. To do this, first the problem is solved for the gas phase, using an implicit coupled pressure-based solver of Navier-Stokes equation, for which its pressure has second-order accuracy. In order to capture the turbulence accurately and with less computational cost, the solution started with a k-ε method, in the first 12,000 iterations, then the turbulence model switched to Reynolds Stress Model (RSM) and it continues to 37,000 iterations while it converges. As discussed by Samareh et al. (Ref 9), using the RSM model provides good agreement in terms of shock capturing and location of Mach stem for the first and second shock diamonds.

After solving the gas phase, the injection of liquid water droplets into the high pressure chamber is simulated by a discrete phase model (DPM). In this model, the droplets are injected through 10 points, each injecting discrete droplets. Essentially the primary breakup, i.e., the breakup of liquid jet into ligaments, is not considered; however, the secondary breakup of droplets to smaller ones is performed by the Taylor Analysis Breakup (TAB) model (Ref 10). Separate simulations are performed for the droplet size distributions described in the previous part.

The spray droplets are tracked with a time step of 0.0001 s and the trajectories of droplets are obtained at every time step. This problem (although steady in nature) is solved using an unsteady solver until time $t = 0.02$ s where beyond this point there was no change in the properties of gas and droplets throughout the computational domain. The evaporation, condensation, or boiling of the droplets is modeled in a two-way coupled simulation to capture both the effect of evaporation on the gaseous field and the effect of changes in the gaseous field on the evaporation of liquid droplets. The species equation also is solved for water vapor species transport in the nitrogen gaseous media with the aim of comparing and modeling evaporation in dry gas and gas with water vapor content. The droplet motion is controlled by the dynamic drag law, which can consider the shape of droplet to be distorted from its original spherical shape. Using the mass-spring concept, the dynamic drag model finds the shape of droplet due to competition of three forces: drag, viscous, and surface tension. The drag coefficient of a spherical droplet in this model is found by Eq 2, and when the droplet is distorted from its original spherical shape, the drag coefficient is given by Eq 3 (Ref 11). The formula for finding the value of nondimensionalized distortion, y, is obtained by the work of Liu et al. (Ref 11) and Lamb (Ref 12) (see Eq 4). The initial value for solving Eq 4, i.e., the value of nondimensionalized distortion of the droplets at the injection point is considered to be $y_0 = 0.1$. It should be mentioned that the distortion is displacement of the droplet equator from its spherical position. The droplet distortion can be nondimensionalized by 0.5 times the radius of the droplet (Ref 13). The nondimensionalized distortion varies between 0 and 1 and, in this study, considering the initial distortion of droplets to be a low value, facilitates the condition for the droplets to breakup or remain unbroken.

$$C_{D_{sphere}} = \begin{cases} 0.424 & Re_d > 1000 \\ \frac{24}{Re_d}\left(1 + \frac{1}{6}Re^{2/3}\right) & Re_d \leq 1000 \end{cases} \quad \text{(Eq 2)}$$

$$C_D = C_{D_{sphere}}(1 + 2.632y) \quad \text{(Eq 3)}$$

$$\frac{d^2y}{dt^2} = \frac{2}{3}\frac{\rho}{\rho_d}\frac{v_d}{R^2} - \frac{8\sigma}{\rho_d R^3}y - \frac{5\mu}{\rho_d R^2}\frac{dy}{dt} \quad \text{(Eq 4)}$$

For modeling heat and mass transfer associated with droplets, three possible scenarios are considered. At each tracking time, the conditions of each scenario are evaluated and the relevant heat and mass transfer laws are applied. These three scenarios are the following: (i) inert heating that happens when the droplet temperature is less than a specified vaporization temperature, e.g., freezing point (see Eq 5), (ii) vaporization which happens when the droplet temperature is greater than the vaporization temperature and less than the boiling temperature (in this scenario, the droplets transfer both heat and mass during the time step, see Eq 6), and (iii) boiling which happens

when the droplet temperature is equal to the boiling temperature (see Eq 7). It should be mentioned that the condition for activating these three scenarios are vaporization, boiling temperature, and saturation pressure. In order to account for temporal and spatial variations, a piecewise linear relation is used for the changes in saturation pressure and vaporization temperature. A user-defined function, based on the Clausius-Clapeyron relation (Ref 14), is written and added to the solver to account for the dependency of boiling temperature on pressure and temperature.

$$m_d c_p \frac{dT_d}{dt} = hA_d(T_\infty - T_d) + \varepsilon_d A_d \kappa\left(\theta_R^4 - T_d^4\right) \quad T_d < T_{vap} \tag{Eq 5}$$

$$\begin{cases} m_d(t+\Delta t) = m_d(t) - \frac{Sh \times D}{2R}(C_s - C_\infty)A_d M_w \Delta t \\ \qquad T_{vap} \le T_p < T_{boil} \quad (a) \\ m_d c_p \frac{dT_d}{dt} = hA_d(T_\infty - T_d) + \frac{dm_d}{dt}L + \varepsilon_d A_d \kappa(\theta_R^4 - T_d^4) \\ \qquad T_{vap} \le T_d < T_{boil} \quad (b) \end{cases} \tag{Eq 6}$$

$$-\frac{dm_d}{dt}L = hA_d(T_\infty - T_d) + A_d \varepsilon_d \kappa\left(\theta_R^4 - T_d^4\right) \quad T_d = T_{boil} \tag{Eq 7}$$

In the above equations, m_d, A_d, and T_d are droplet or particle mass, surface area, and temperature, respectively, c_p is the droplet heat capacity, and ε_d, κ, and T_∞ are droplet emissivity, Stefan-Boltzman radiation constant and gas temperature, respectively. Furthermore, θ_R is radiation temperature, and h, L, and Sh are convective heat transfer coefficient, latent heat of evaporation and Sherwood number, respectively. It should be noticed that C_s and C_∞ are vapor concentration at the droplet surface and vapor concentration at bulk gas, respectively. Sh in the above equation is calculated using a semi-empirical relation as follows:

$$Sh = 2 + 0.6 Re_d^{0.5} Sc^{1/3} \tag{Eq 8}$$

4. Results

4.1 Effect of Liquid Feedstock on Gaseous Flow

The results of the gas phase modeling, including the locus of shock diamonds, showed a good agreement with the experimental results as extensively discussed in the recent work of the authors (Ref 9). Therefore, those results will not be further analyzed here. The main aim of this article is to numerically track the injected droplets while evaporating, and consequently determine their effects on the main gas flow to provide a feasibility of using liquid suspensions in a cold spray.

The crucial criterion in cold spray application is to have high gas and particle velocity at the nozzle exit. Owing to this fact, the supersonic gas field should be guaranteed in the diverging section of the nozzle. This requires that the flow be choked (i.e., sonic flow at the throat), while a high amount of water vapor along with the gas flow passes through the nozzle throat. Hence, as in the first investigation, two working back pressures of 40 and 24 bars for the inlet gas, have been simulated using different liquid injection flow rates. The choking at the throat is examined as a function of gas to liquid mass ratio (GLR). The result of this study is summarized in Table 1 which shows that choking is guaranteed for GLRs of greater than 5.1.

Using the above criterion for choked nozzle, the following numerical results are presenting the inlet gas pressure of 40 bars and the liquid mass flow rates of 1, 3, and 5 g/s. The results of gas temperature and pressure with 1 g/s water injection using a uniform droplet size of 30 μm are shown in Fig. 3 and 4. The contours of temperature

Table 1 Assessment of choking for different GLRs

P, bar	m_g', g/s	m_l', g/s	GLR	Choked/not choked
40	30.8	1	30.8	Choked
40	30.8	3	10.3	Choked
40	30.8	5	6.16	Choked
40	30.8	5.5	5.6	Choked
40	30.8	6	5.1	Choked
40	30.8	6.5	4.7	Not choked
40	30.7	7	4.4	Not choked
24	19.5	1	19.5	Choked
24	19.5	3	6.5	Choked
24	19.5	3.5	5.6	Choked
24	19.4	4	4.9	Not choked
24	19.4	4.5	4.3	Not choked
24	19.3	5	3.9	Not choked

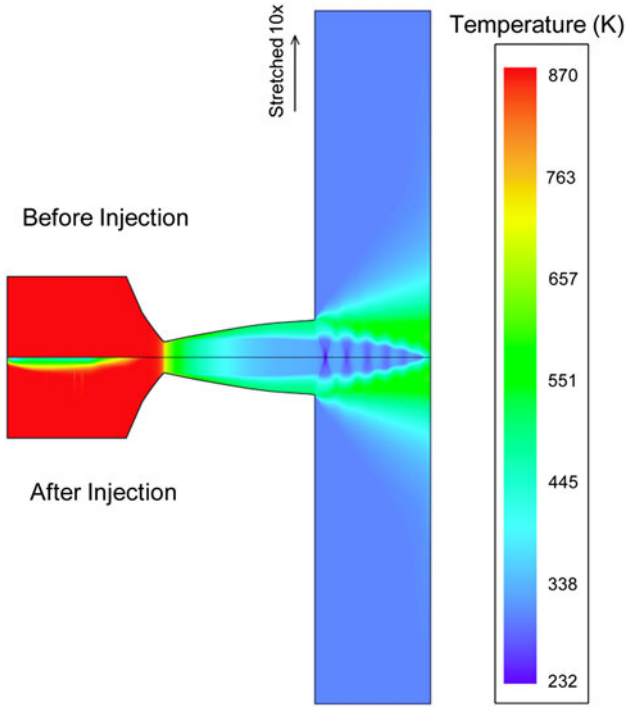

Fig. 3 Gas temperature contours before and after the water injection

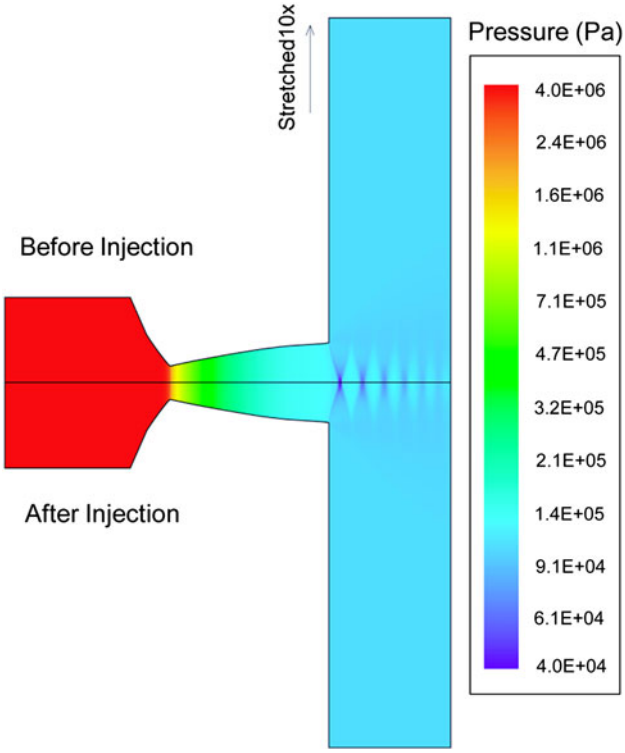

Fig. 4 Gas pressure contours before and after the water injection

and pressure before injection are shown on the top and the contours of temperature and pressure after the injection of water droplets are shown on the bottom of each figure.

According to the temperature contours of Fig. 3, water droplet injection has a considerable effect on the temperature contours inside the high pressure chamber in the vicinity of the axis, but through the nozzle, this effect decreases and it vanishes almost completely after the throat section. Starting with the converged steady gas flow solution, the droplets are injected to the nozzle inlet. The water droplets travel through the nozzle, evaporate, and result in a transient temperature change in the gas as a cause of heat and mass transfer. The two-phase flow becomes almost steady after $t = 0.01$ s, and, to ensure the convergence, the simulation was carried out until $t = 0.02$ s.

The temperature change in gaseous flow is expected because the temperature difference right after the injection is very high (about 573 K), where the droplets start to heat up and evaporate. Through the nozzle converging-diverging part, the gas flow expands very rapidly and hence the gas temperature decreases at a fast rate. Using a lumped heat capacity system for the droplet (*Bi* number is in the order of 10^{-4} to 10^{-3}), the time response constant for the droplet is in the order of 10^{-1} s while the time required for the droplets and gas to travel through the nozzle is in the order of 10^{-4} s. This means that the droplet temperature does not change remarkably, especially in the diverging section of the nozzle. Figure 4 shows that water droplet injection has almost no effect on

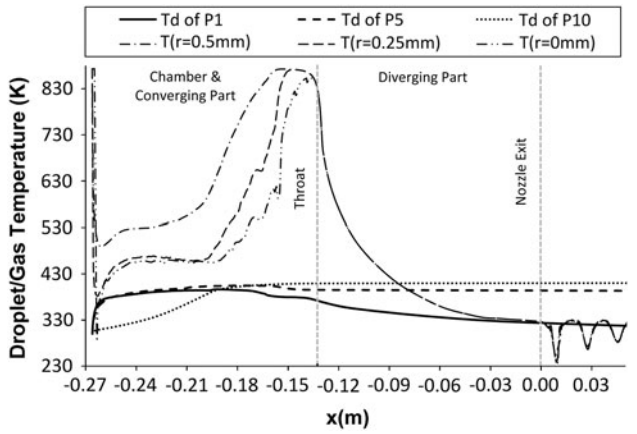

Fig. 5 Droplets temperature variations through the chamber and nozzle (initial droplet size: 50 μm, flow rate: 1 g/s)

the pressure contours and consequently on the shock diamond configuration in general.

Figure 5 shows the droplet temperature variations from the injection point to the nozzle exit. Generally, the temperature increase rate is very steep just after the injection, where there is a large temperature difference between the gas and droplets. This rate plateaus after some traveling of the droplets, because of the reduction of gas-droplet temperature difference and/or of having fast velocities and long time scales of heat transfer in the converging-diverging part of the nozzle. The figure also shows that from the converging section of the nozzle, the droplets have started to cool down. This behavior as discussed above is a consequence of gas expansion and gas temperature reduction.

It is important to mention that at the nozzle throat or even at the converging part, the gas temperature is about 873 K (Fig. 3) and droplets there are at a lower temperature (about 370 K, Fig. 4). In this case, the energy balance for the droplet is governed by both convection and evaporation (Eq 6b). While heating up by the surrounding gas, the droplets are cooled down due to the evaporation, which results a reduction in droplet temperature. Additionally, at the entry of the converging part of the nozzle, as can be seen in Fig. 5, the steep rates of droplet cooling are mainly because of augmented *Re* and *Sh*.

Another important issue that might be affected by the droplets, especially in a cold spray nozzle, is the gas Mach number. The gas Mach number can directly influence the coating particle velocity. The numerical results of the nozzle before and after injection in Fig. 6 show that the gas Mach number through the whole nozzle and especially after the throat, where there exist shock diamonds, is almost identical to the gas Mach number of the single-phase simulation. This means that as long as the choking condition is provided at the throat, the water injection has almost no effect on the gas Mach number. The results presented in Fig. 3 and 4 confirm this argument by showing that the gas temperature and pressure contours after the throat remained almost unchanged before and after the injection.

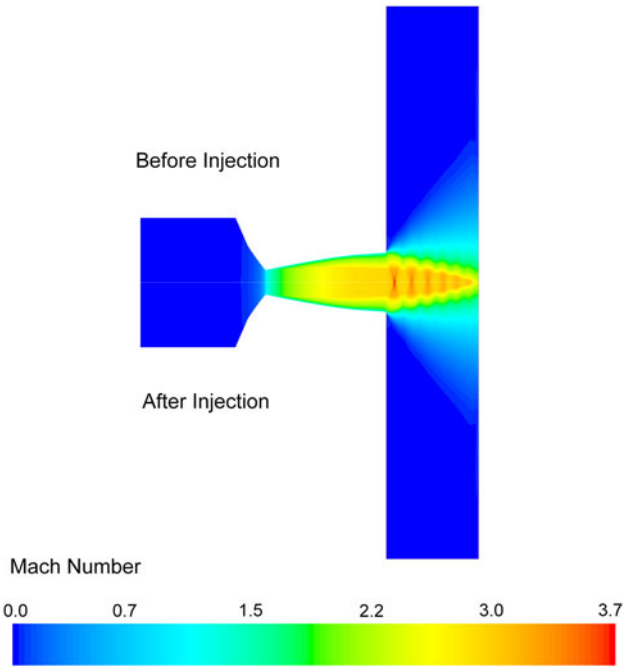

Fig. 6 Mach number contour before and after injection

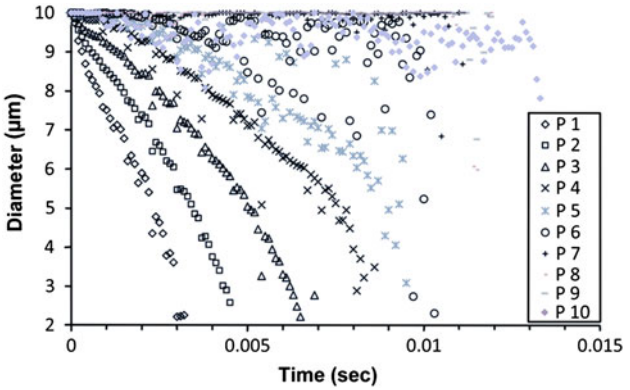

Fig. 7 Variation of droplet diameter released from various radial locations (initial diameter: 10 μm, flow rate: 1 g/s)

4.2 Liquid Droplets Evaporation

4.2.1 Liquid-Gas Coupled CFD Simulation. In addition to the effect of water injection on the main gaseous flow, the spray droplets undergo simultaneous breakup and evaporation processes. In fact, the most important investigation for application in cold spray is the suspension spray evaporation rate which can predict the evaporation of liquid part. Diameter variation of 10 μm droplets injected through locations P1 to P10 due to evaporation is indicated in Fig. 7.

Figure 8 and 9 are used to demonstrate the dependency of droplet initial diameter on the evaporation rate of droplets injecting through locations P1 and P5, respectively. To obtain these plots, numerical simulations are performed with 10, 30, and 50 μm droplet diameters injected from P1 to P10. In contrast to results shown in

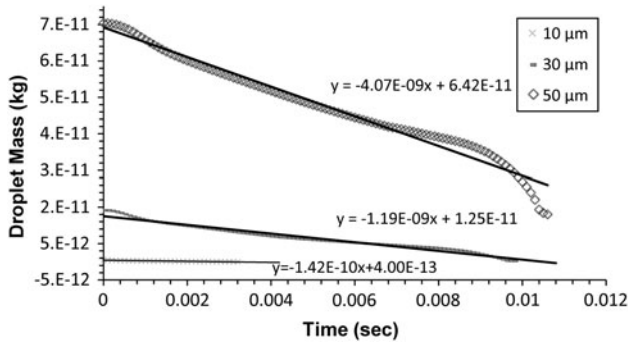

Fig. 8 Effect of initial droplet size on the evaporation rate of droplets injected from P1 (flow rate: 1 g/s)

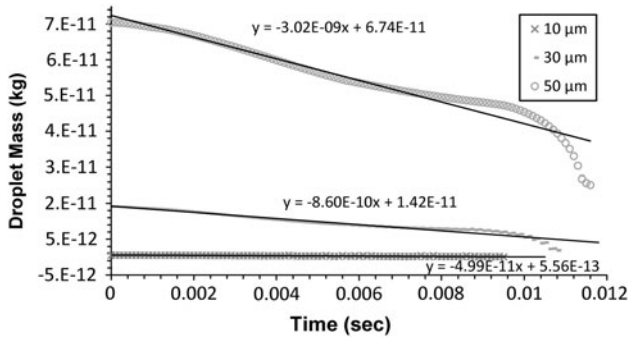

Fig. 9 Effect of initial droplet size on the evaporation rate of droplets injected from P5 (flow rate: 1 g/s)

Fig. 7, in which the rate of change of droplet diameter is nonlinear and variable with time, in Fig. 8 and 9, the rate of evaporation is almost constant and therefore the diagrams can be fitted with a line.

Another important factor affecting the rate of evaporation is the total liquid mass flow rate. Figure 10 shows the evaporation rate of droplets injected from port 1 and having the initial diameter of 10 μm. It is evident that the higher the mass flow rate, the lower the evaporation rate. In fact increasing the liquid mass flow rate, while the droplet diameter is kept constant, is to increase the droplet velocity and to decrease the relative velocity between gas and droplet which results in a lower evaporation rate.

4.2.2 Semi-Empirical Verification. A semi-empirical correlation that estimates the change of diameter is presented by Hallet et al. (Ref 15),

$$\frac{dR}{dt} = -\left(1 + \frac{0.277 Re_d^{0.5} Sc^{0.333}}{1 + \frac{1.232}{Re_d Sc^{1.333}}}\right) \frac{\rho D}{\rho_d R} \ln(1 + B) \qquad \text{(Eq 9)}$$

$$\frac{dm_d}{dt} = -\left(1 + \frac{0.277 Re_d^{0.5} Sc^{0.333}}{1 + \frac{1.232}{Re_d Sc^{1.333}}}\right) (4\pi R \rho D) \ln(1 + B) \qquad \text{(Eq 10)}$$

where R is the droplet radius, ρ is the gas density, ρ_d is the droplet density, D is the binary diffusivity of gas-droplet, $B = (Y^* - Y_l)/(1 - Y^*)$, and $Y^* = P_l^{sat}(T_d)/P$ is mass fraction of liquid at droplet surface, and Y_l is the mass fraction of liquid at the bulk gas.

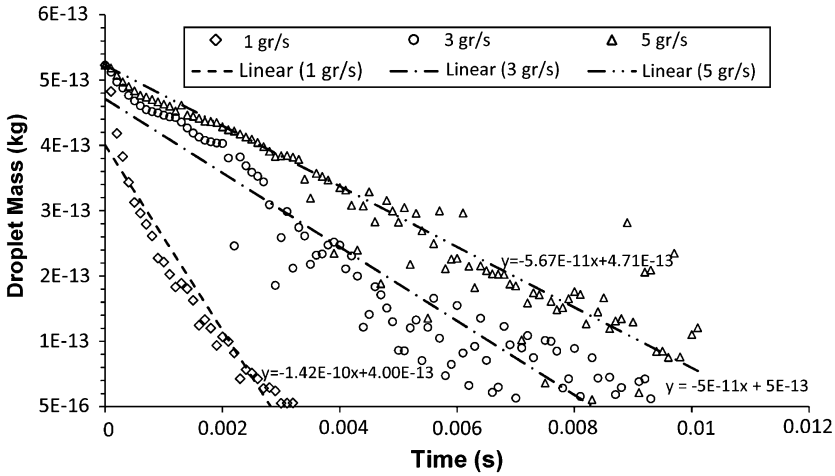

Fig. 10 Effect of liquid mass flow rate on evaporation rate of droplets injected from P1 ($d_0 = 10$ μm)

According to Eq 9 (considering value in brackets to be constant), the second derivative of droplet diameter with respect to time is negative which verifies the concave downward plots shown in Fig. 7. Additionally, the slope of the graph becomes larger as diameter decreases in time. It should be noticed in Fig. 7 that all droplets injected from locations P1 to P10 have the same initial diameter of 10 μm at the injection point, but their diameter-time graphs are different from each other. This difference can be more clarified using Eq 9, as it implicitly contains two other effects. The first one is the radial temperature gradient of gas from P1 to P10 which affects Y^*, and the second one is the water vapor content in the neighboring gas flow which is different for P1 to P10 and influences the value of Y_1. For example, P1 encounters more dried gas because it is the outermost particle, while P10 is surrounded with a gas flow with maximum water content.

On the other hand, using Eq 9 and assuming constant droplet density, it is evident that the droplet mass is proportional to the cube of diameter. Hence, the differentiation of droplet mass yields Eq 10.

It is important to mention that the values of Re, Sh, and B in Eq 10 vary with time as a consequence of a change in droplet diameter, velocity, and temperature, as well as variation of vapor content in the bulk gas. Hence, to use the semi-empirical Eq 10, a set of semi-empirical equations are required to model the variations of velocity, temperature, and vapor content in the bulk gas. To account for the velocity variations, Henderson (Ref 16) suggested the drag coefficient for particles and/or droplets as presented in Eq 11.

$$C_D = \frac{24}{Re_d + 3.06\sqrt{M_d}} + \frac{4.5 + 0.0114Re_d + 0.1825\sqrt{Re_d}}{1 + 0.03Re_d + 0.48\sqrt{Re_d}} + 0.1M_d^2 + 0.2M_d^8 \quad \text{(Eq 11)}$$

where $Re_d = \rho(v - v_d)d/\mu$ and $M_d = |v - v_d|/a$. The drag coefficient can be used in the droplet momentum equation to find the velocity variation.

$$\rho_d \frac{\pi d^3}{6}\frac{dv_d}{dt} = C_D \frac{\rho(v - v_d)^2}{2}\frac{\pi d^2}{4} \quad \text{(Eq 12)}$$

Since the drag coefficient is related to Reynolds and Mach numbers, therefore it should be coupled with a temperature variation relation. In order to account for the variation of temperature, Kim et al. (Ref 17) suggested using a combination of Spalding (Ref 18) form of energy conservation and semi-empirical Nusselt equation by Ranz et al. (Ref 19). In this form of energy conservation, the radiation heat transfer is neglected and the energy equation becomes the convection heat transfer of gas to droplet equals the heat of evaporation plus the inert heating of the droplet.

$$\pi dk(T - T_d)Nu_d = \frac{dm_d}{dt}L + m_d c_p \frac{dT_d}{dt} \quad \text{(Eq 13)}$$

$$Nu_d = \left(2 + 0.6Re_d^{0.5}Pr^{0.333}\right)\frac{\ln(1 + B)}{B} \quad \text{(Eq 14)}$$

In order to evaluate and compare the numerical simulation results with the semi-empirical correlations, a coupled set of Eq 9 to 14 is solved to find the evaporation rate of droplets. To do this, the set of equations is solved in a separate numerical one-dimensional code by discretization in time using a time step of 0.00001 s. The one dimensionality does not significantly influence the results of Eq 9 to 14, because the radial and azimuthal components of droplet velocities are negligible when compared to the axial velocity of droplets. The injections in cold spray nozzles are usually within a narrow area of the axis and the particles or droplets usually pass along a narrow region of the nozzle with a very small radial velocity. Back to the semi-empirical set of equations, in time zero the droplet is considered with an initial condition of diameter, temperature, velocity, surface humidity, and radial location. After each time step, first the droplet Reynolds and Mach numbers are calculated using the relative velocity, temperature, and surface humidity in the previous time step (Euler forward discretization). Subsequently, the

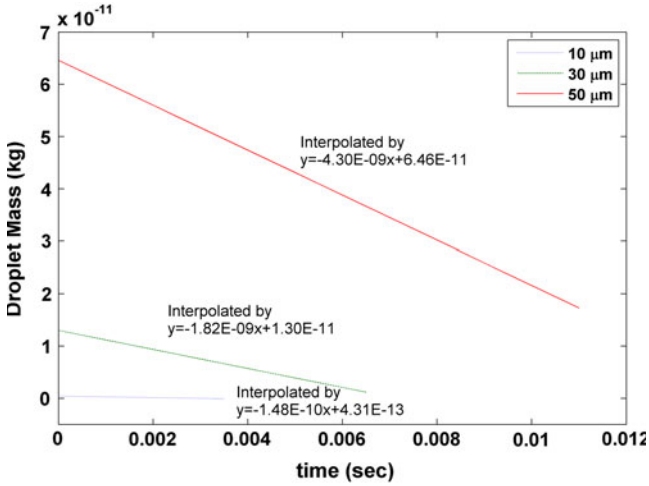

Fig. 11 Effect of initial droplet size on the evaporation rate of droplets injected from P1, found by semi-empirical correlations (flow rate: 1 g/s)

velocity, diameter, and temperature are updated for $t+\Delta t$ using the set of empirical equations. Having the difference in diameters at time t and $t+\Delta t$, the evaporated mass is calculated and is considered to be diffused in the adjacent cell. This evaporated mass in turn affects the value of B and sound speed in the next time step. The results of this set of empirical relations for the evaporation rate of droplets injected through P1 are illustrated in Fig. 11.

It is clear from Fig. 8 and 11 that the results by both methods have agreement and generally the empirical correlations predict a linear profile for evaporation of droplets in time. So it can be inferred that although evaporation rate is proportional to the droplet diameter and diameter varies with time, the value of evaporation rate is constant. Therefore it seems that the results of changing B, Reynolds and Schmidt numbers totally nullify the effect of diameter in Eq 10, so that the right-hand side becomes almost constant with time. An additional interesting observation is that the rate of evaporation is proportional to the square of initial diameter. For example, as can be seen in Fig. 8 and 11, the rate of evaporation of a 30 μm injected droplet is almost nine times the evaporation rate of a 10 μm droplet.

4.3 Trajectory and Evaporation of Suspension Droplets

Considering the verified CFD results of evaporation, Fig. 12 summarizes the evaporation procedure and trajectory of droplets injected uniformly with the diameters of 20, 30, and 50 μm. As mentioned before and can be seen in each part of this figure, the evaporation rate of the droplets injected from port 1 is the highest while that of those injected from port 10 is the lowest. Keeping in mind the applied advantage of having evenly distributed evaporation, one can use the results of this figure to design the injectors for injecting higher mass flow ratios or larger droplet diameters in ports located on the periphery and lower mass flow rates or smaller droplet diameters in ports located near the axis.

The simulation results of three different droplet sizes (i.e., 20, 30, and 50 μm) injected from ports P1 to P10 are illustrated in Fig. 13. The figure represents the average droplet diameters injected from P1 to P10 along the nozzle axis.

Considering Fig. 12 and 13, the 20 μm injected droplets fully evaporate in a short distance inside the high pressure chamber. The 30 μm droplet evaporates in the chamber, but the evaporation is not complete before it reaches the nozzle throat. The result of simulation shows that the 30 μm injected droplet becomes a droplet with a size of 9 μm when it reaches the throat and then from the throat up to the nozzle exit, its diameter reduces to 7 μm. In other words, the 30 μm injected droplet experiences more than 98% (by volume) of the total evaporation before the throat. Furthermore, the 50 μm injected droplet also partially evaporates in the chamber and in the converging part of the nozzle, its size reduces to 34 μm while passing the throat and then up to the nozzle exit, its diameter becomes 31 μm. Again this means that the 50 μm injected particles experience more than 90% (by volume) of the total evaporation before the throat. The possible causes of this evaporation behavior as reasoned in the preceding paragraphs are firstly, the drastic decrease of gas-droplet temperature difference through the nozzle and secondly, the higher velocities and short times associated with heat and mass transfer. Consequently, it can be conferred that in suspension or solution sprays in high pressure cold spray nozzles, most of liquid evaporation occurs before the throat. Therefore, for having a feasible coating process which requires fully evaporated droplets, i.e., dried solid particles with no water droplet leaving the nozzle, the process should be prepared so that the liquid part of the suspension fully evaporates before the throat. In other words, due to high expansion of the gaseous phase in the nozzle, having residual humidity in the particles passing the throat may result in freezing that is not desirable.

As a rather simple and straightforward approach, this can be achieved if for a specific injection size, the suspension volumetric solid to liquid fraction is considered to be equal to the volume ratio of the droplet passing the throat to the droplet initially injected. For example, see Fig. 14, if in a cold spray nozzle the injector delivers predominantly, 50 μm droplets (Sauter mean diameter of the injector), the minimum solid to total volume ratio should be about 30%. Conversely, for coating with a suspension of 30% solid to the total volume of suspension (in case of water as the liquid part of suspension), the injector Sauter mean diameter should be maximum 50 μm.

5. Conclusions

A preliminary study has been performed on water injection into high pressure cold spray nozzles to provide an overview of the feasibility of using suspension sprays.

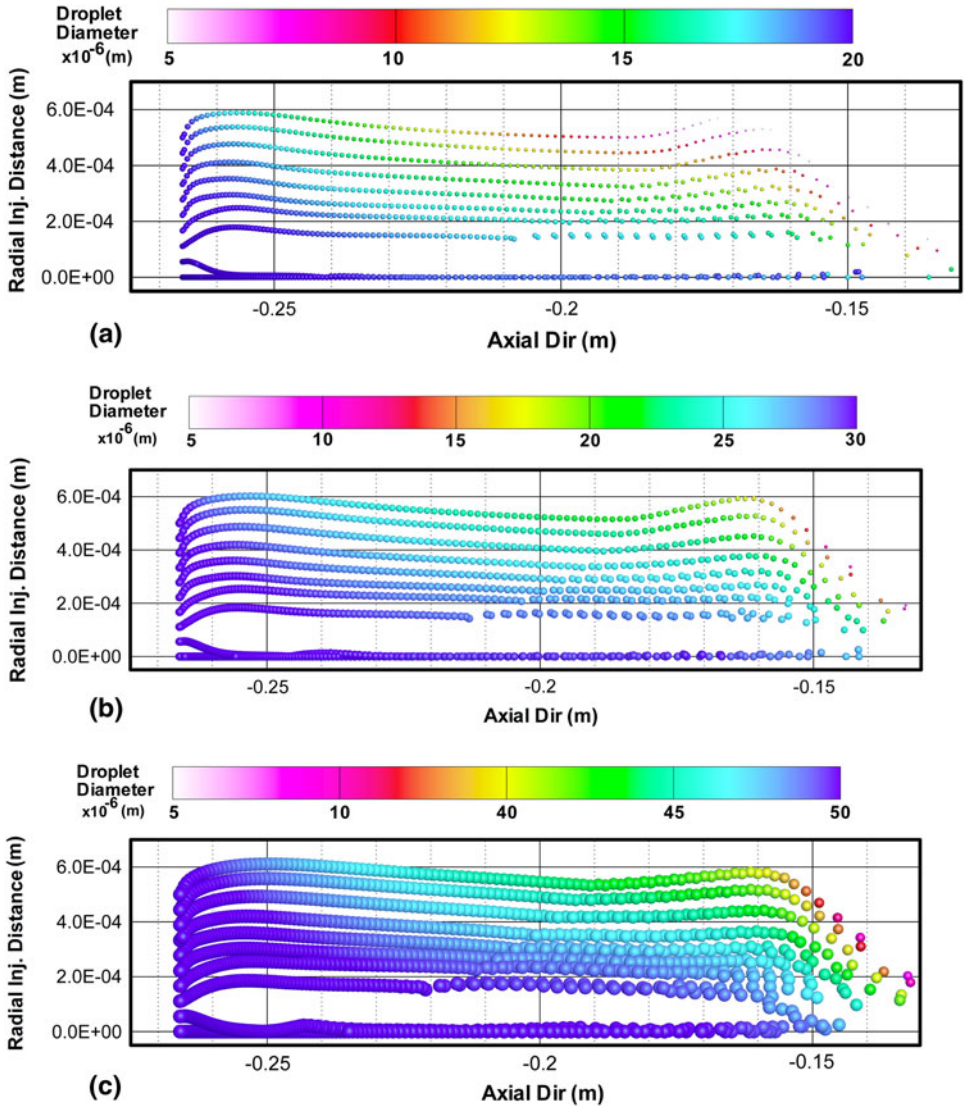

Fig. 12 Evaporation of different size of droplets along their trajectory (flow rate: 1 g/s (a) $d_0 = 20$ μm, (b) $d_0 = 30$ μm, (c) $d_0 = 50$ μm)

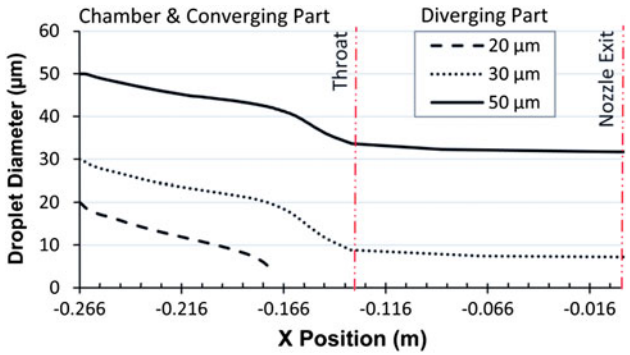

Fig. 13 Average diameter of droplets injected from all ports versus axial position

In this study, the ratio of spray to gas, whether liquid or suspension, is considered low to moderate, so that choking of the nozzle is guaranteed throughout the study. Results show that the evaporation of spray causes a temperature gradient in a periphery of the axis of the high pressure chamber; however, this temperature gradient vanishes around the beginning of the converging part of the nozzle, so that the temperature field after the throat is not affected by the spray. On the other hand, pressure contours remain almost unchanged all over the nozzle. The Mach number of the gaseous flow after the throat also is not affected by the spray evaporation. As a matter of fact, this behavior is a result of spray evaporation before the throat, while spray does not evaporate remarkably after that. Therefore it is suggested to adjust the solid concentration in the suspension so that the liquid part can be evaporated before the throat. In another attempt, the evaporation rate of spray is estimated both numerically and semi-empirically and the results show a linear evaporation of spray with time. Having the evaporation rate of the droplets and its diameter ratio at the injection point to the nozzle exit, the remaining part of the droplets which

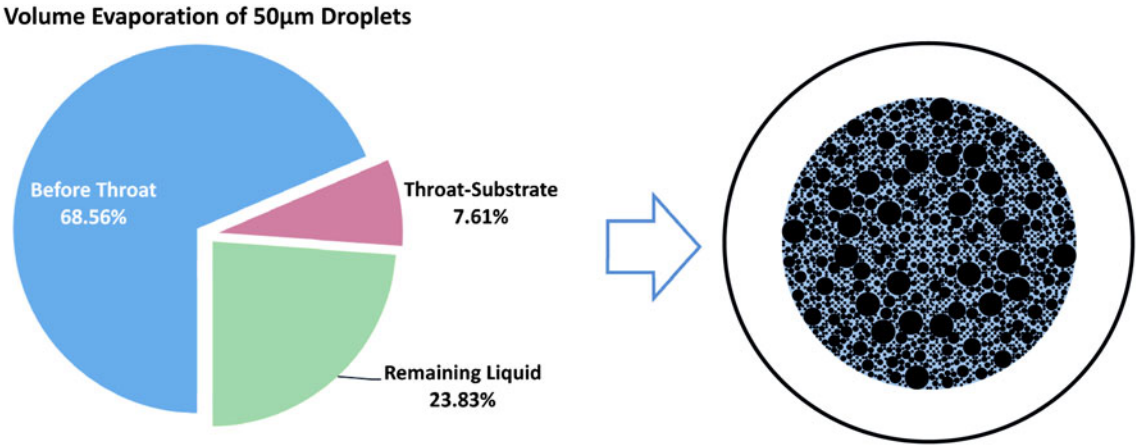

Fig. 14 Volume evaporation of 50 μm injected droplets, along the nozzle to determine the minimum fraction of nanoparticle

leave the nozzle can be substituted by solid parts, namely the nano-particle agglomeration. Finally, the results of this study can serve as a design for suspension injection into a high pressure cold spray nozzle. They can be used to determine the minimum volumetric fraction of solid to liquid part of suspension which guarantees a fully evaporated liquid spray.

Acknowledgment

The first and last authors would like to thank Siemens, AG, Berlin and Natural Sciences and Engineering Research Council of Canada (NSERC) for their financial supports.

References

1. F.V. Shaw, Spray Drying as an Alternative Granulation Technique, *Handbook of Pharmaceutical Granulation Technology, Drugs and the Pharmaceutical Sciences*, 1st ed., D.M. Parikh, Ed., Marcel Dekker, 1997, p 75-96
2. L. Pawlowski, Suspension and Solution Thermal Spray Coatings, *Surf. Coat. Technol.*, 2009, **203**(19), p 2807-2829
3. S.R. Taylor and K. Sieradzki, The Development of a Multi-Functional Aerospace Coating: Considerations in The Use of Nano-Dimensioned Materials, *Prog. Org. Coat.*, 2003, **47**(3-4), p 169-173
4. Z. Wang, E. Han, and W. Ke, An Investigation into Fire Protection and Water Resistance of Intumescent Nano-Coatings, *Surf. Coat. Technol.*, 2006, **201**(3-4), p 1528-1535
5. S. Veprek and M.J.G. Veprek-Heijman, Industrial Applications of Superhard Nanocomposite Coatings, *Surf. Coat. Technol.*, 2008, **202**(21), p 5063-5073
6. J. Fazilleau, C. Delbos, V. Rat, J.F. Coudert, P. Fauchais, and B. Pateyron, Phenomena Involved in Suspension Plasma Spraying Part 1: Suspension Injection and Behavior, *Plasma Chem. Plasma Process.*, 2006, **26**(4), p 371-391
7. J.O. Berghaus, B. Marple, and C. Moreau, Suspension Plasma Spraying of Nanostructured WC-12Co Coatings, *J. Therm. Spray Technol.*, 2006, **15**(4), p 676-681
8. A. Esfarjani and A. Dolatabadi, A 3D Simulation of Two-Phase Flow in an Effervescent Atomizer for Suspension Plasma Spray, *Surf. Coat. Technol.*, 2009, **203**(15), p 2074-2080
9. B. Samareh, O. Stier, V. Luthen, and A. Dolatabadi, Assessment of CFD Modeling via Flow Visualization in Cold Spray Process, *J. Therm. Spray Technol.*, 2009, **18**(5-6), p 934-943
10. G. I. Taylor, The Shape and Acceleration of a Drop in a High Speed Air Stream, *Scientific Papers of G. I. Taylor*, 1st ed., G.K. Batchelor, Ed., Cambridge University Press, 1963, p 457-464
11. A.B. Liu, D. Mather, and R.D. Reitz, "Modeling the Effects of Drop Drag and Breakup on Fuel Sprays," SAE Technical Paper 930072, SAE, 1993
12. H. Lamb, Surface Waves, *Hydrodynamics*, 6th ed., Dover Publications, New York, 1945
13. P.J. O'Rourke and A.A. Amsden, "The TAB Method for Numerical Calculation of Spray Droplet Breakup," SAE Technical Paper 872089, SAE, 1987
14. Y.A. Cengel and M. Boles, Thermodynamic Property Relation, *Thermodynamics: An Engineering Approach*, 5th ed., McGraw Hill, 2005, p 658-661
15. L.H. Hallett, A Simple Model for the Vaporization of Droplets with Large Numbers of Components, *Combust. Flame*, 2000, **121**(3), p 334-344
16. C.B. Henderson, Drag Coefficient of Spheres in Continuum and Rarefied Flows, *AIAA J*, 1976, **14**(6), p 707-708
17. H. Kim and N. Sung, The Effect of Ambient Pressure on the Evaporation of a Single Droplet and a Spray, *Combust. Flame*, 2003, **135**(3), p 261-270
18. D.B. Spalding, The Combustion of Liquid Fuels, *Fourth Symposium (International) on Combustion*, 1954 (Pittsburgh, PA), The Combustion Institute, 1954, p 847-864
19. W.E. Ranz and W.R. Marshall, Evaporation from Drops, *Chem. Eng. Prog.*, 1952, **48**(3), p 141-146, 173-180